Cascade processes and the kinetic-energy distribution of pionic hydrogen atoms

E. C. Aschenauer,* K. Gabathuler, P. Hauser, and J. Missimer
Paul Scherrer Institut, CH-5232 Villigen PSI, Switzerland

A. Badertscher, P. F. A. Goudsmit, H. J. Leisi, H.-Ch. Schröder, D. Sigg, and Z. G. Zhao
Institute for Particle Physics, Eidgenössische Technische Hochschule Zürich, CH-5232 Villigen PSI, Switzerland

D. Chattellard and J.-P. Egger
Institut de Physique de l'Université de Neuchâtel, CH-2000 Neuchâtel, Switzerland

V. E. Markushin
Russian Research Center, Kurchatov Institute, Moscow 123182, Russia
(Received 19 July 1994)

The previously unmeasured neutron time-of-flight distributions for the reaction $\pi^- p \to \pi^0 n$ in gaseous targets at pressures of 17 and 40 bar have been measured. The kinetic energy of the $\pi^- p$ atoms at the instant of the nuclear reaction has been evaluated from the Doppler broadening of the neutron time-of-flight spectra. Evidence was found for $\pi^- p$ atoms with kinetic energies of 75 eV. The present experimental data were interpreted within a cascade model that takes the evolution of the kinetic-energy distribution during the cascade into account. The parameters of the model were determined from experiments measuring neutron time of flight in liquid hydrogen and x-ray yields in gas. Coulomb deexcitation is responsible for the significant fraction of the high-energy component, whose intensities are compatible with the calculations of Bracci and Fiorentini [Nuovo Cimento **43A**, 9 (1978)]. Stark mixing is found to be significantly stronger than in the commonly used straight-line approximation; the initial mean kinetic energy of 1–2 eV is consistent with the results of muonic hydrogen. The model therefore describes the cascade of pionic hydrogen over a range of pressures of three orders of magnitude. The implications for high-resolution x-ray measurements of the 1*S*-level nuclear width are discussed.

PACS number(s): 36.10.−k

I. INTRODUCTION

The pionic hydrogen atom is the simplest exotic atom formed with pions, and has been studied both theoretically [1–3] and experimentally [4–8] for many years. The measurement of pionic hydrogen x rays is the main method of investigating the pion-nucleon interaction at zero energy [9,10]. The evaluation of the strong interaction width requires knowledge of the Doppler broadening of the x-ray line due to the finite kinetic-energy distribution of the pionic atom at the instant of the radiative transition.

The importance of the kinetic-energy distribution was first demonstrated by the precision measurement of the pion mass difference $m_{\pi^-} - m_{\pi^0}$ [8] at liquid-hydrogen density (LHD), which found that a significant fraction (44%) of $\pi^- p$ at the instant of absorption has a kinetic-energy distribution extending up to about 70 eV. In Sec. II we present a measurement of the time-of-flight (TOF) distribution of the neutrons from the charge-exchange reaction. In contrast to the experiment done in liquid hydrogen [8], our measurements were performed with hydrogen gas at pressures of 17 and 40 bar, corresponding to the pressure range at which absolute *K*-shell x-ray yields were also measured [11].

The kinetic-energy distribution obtained in these experiments results from the deexcitation processes in the atomic cascade. Some basic features of the cascade, including the density dependence of the x-ray yields and the cascade time, can successfully be described by the standard cascade model introduced in [1] (see [3,12,13] and references therein). The kinetic energy of the atom T is treated as a fixed fitting parameter in the calculations of energy-dependent cascade processes (typically $T \sim 1$ eV).

In order to provide a detailed theoretical background for current and future studies of the light exotic atoms, a cascade computer code has been developed [14] which provides a description of the time evolution of the kinetic-energy distribution. The kinetic-energy distribution at the instant of absorption is not the only result of the present model. Incorporating the experimental data on *K*-shell x-ray yields [11] and neutron time of flight (NTOF) at pressures of 17, 40, and 780 bar, the model provides a description of the cascade for a range of pressures over three orders of magnitude in terms of three parameters. In Sec. III we discuss this model and introduce the three parameters: an initial kinetic energy and two correction factors describing uncertainties in calculations

*Present address: NIKHEF-K, P.O. Box 41882, NL-1009 DB Amsterdam, The Netherlands.

of Stark mixing and Coulomb deexcitation.

In Sec. IV we determine the cascade model parameters by means of the K-shell x-ray yields [11] and the NTOF in liquid hydrogen [8]. One result of the analysis is that Stark mixing rates calculated in the straight-line approximation according to [1,3], even with the corrections of Ref. [15], are too small to describe the data properly. From the kinetic-energy fractions deduced from the NTOF experiments, two of the three existing theoretical calculations [16–18] of Coulomb deexcitation rates can be excluded.

Section V discusses the implications of the kinetic-energy distribution for the Doppler broadening of the x-ray line in high-resolution spectroscopy [20]. We compare the results on the muonic and pionic cascades. A new experiment with muonic atoms which could provide information about the kinetic-energy distribution is discussed. Prospects for future improvements of NTOF measurements are also given.

II. NEUTRON TIME OF FLIGHT

A. Experimental setup

The experimental setup (Fig. 1) used to measure the time of flight of the neutron from the charge-exchange reaction, $\pi^- p \rightarrow \pi^0 n$, is an extension of that used to measure K-shell x-ray yields as a function of gas pressure [11]; the additional component was a neutron detector. The measurements were performed at the $\pi E3$ area of the Paul Scherrer Institute (PSI). The chosen momentum of the pion beam was 80 MeV/c with a momentum band of $\pm 5\%$. In order to stop a sufficient number of pions in a very small volume at relatively low pressures (17 and 40 bar at normal temperature) in a hydrogen target, use was made of the "cyclotron trap" [21]. After injection into the trap, the pion beam was transported through the fringe field to the beam monitor ($S1$), a plastic scintillator of 10-mm thickness and 10-mm axial width. The scintillator was designed to select a portion of the beam which produced a small stop distribution at the center of the cyclotron trap; the small stop distribution was essential for good time resolution. In front of the beam monitor was placed a 12-mm-thick CH_2 degrader. This degrader together with a series of other CH_2 degraders behind the monitor moderated the pions to momenta of about 30 MeV/c. The beam was thus optimized to form pionic hydrogen in a cylindrical gas target (∅ 60 mm, collimated length 10 mm) [11,22] located at the center of the cyclotron trap.

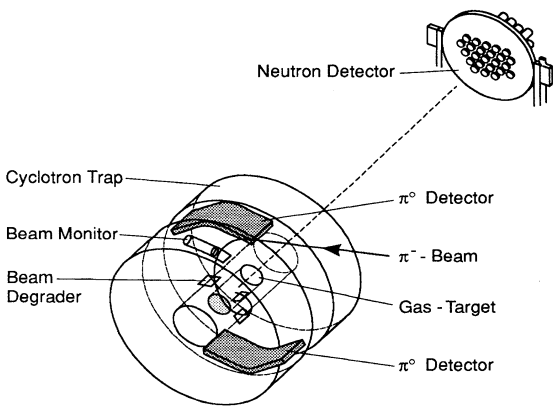

FIG. 1. Experimental setup for the neutron time-of-flight measurement.

The π^0 was identified via detection of one of its two decay photons in the π^0 detector placed around the target within the gap of the trap. In our setup the neutron detector (NC) was oriented at 90° with respect to the beam direction in order to suppress background from bremsstrahlung. The time of flight was defined by the time difference between detection of one of the π^0 photons and a neutron.

1. *The neutron detector*

The neutron detector [23] consisted of 26 Pilot U plastic scintillators, each with a diameter of 44 mm and a thickness of 12 mm, mounted in a hexagonal array on a spherical surface with focus at the target cell. The Pilot U scintillators were chosen because of their good time resolution; an intrinsic resolution of 1.2 ns [full width at half maximum (FWHM)] for a single neutron counter was measured using different sources (^{60}Co, ^{133}Ba, and ^{137}Cs). The scintillators were glued directly onto the XP2020 photomultipliers. The solid angle acceptance of the neutron detector positioned 6 m from the center of the cyclotron trap was 0.9 msr; the calculated efficiency of the scintillators for detecting a 420-keV neutron was 19%.

2. *The π^0 detector*

The π^0 detector [23] consisted of two sandwich counters ($\gamma_{up}, \gamma_{down}$) constructed of tungsten and scintillating fibers with a total thickness of six radiation lengths. The scintillating fibers were read out on both sides of XP2020 photomultipliers. The detector covered a solid angle of 1.81 sr (14.4% of 4π) and detected 5% of the π^0's produced at rest at the center of the trap. The Panofsky ratio and the kinematic constraint imposed by the neutron flight direction then implied that the fraction of $\pi^- p$ atoms yielding coincident π^0's was 1%. The two detector parts were placed in the gap of the cyclotron trap. We originally planned to use both sandwich counters in coincidence to define a clean signal for an emitted π^0. However, the count rate in the lower detector caused by the electron contamination of the beam was too high to yield a useful coincidence. Fortunately the peak-to-background ratio using the upper detector alone was good enough to obtain a useful NTOF spectrum. The data presented below were thus obtained using single-photon detection. The time resolution was checked on-line using the beam electrons, and was measured to be 3 ns; this was the dominant contribution to the total time resolution. Details of the analysis are presented in Sec. II D.

B. Electronics

The neutron time-of-flight spectrum was measured using the trigger scheme sketched in Fig. 2.

The initial time was defined by detecting one of the two photons from the π^0 decay. To reduce background in the trigger, the CAMAC look-at-me (LAM) signal was formed by a coincidence of the $S1$, γ_{up} or γ_{down}, and the neutron counters. In addition the "TDC π-Stop" signal (Fig. 2) recorded the time between π^- passing $S1$ and forming a $\pi^- p$; this information was used to further reduce background in the later analysis. The analog-to-digital conversion (ADC) spectra from each single neutron detector, from $S1$, and from γ^+_{up}, γ^-_{up}, γ^+_{down}, and γ^-_{down} (+ denotes in the beam direction, − denotes against the beam direction) were taken to enable background reduction and resolution improvements in the off-line analysis (Sec. II D).

As the data-acquisition system, the PSI standard TANDEM was used [24]. It consists of a front-end processor (ACC 2180 from CES) housed in a CAMAC electronics crate which reads data from the modules and sends them over a DECNET link to a VAX/VMS computer. Here the data were analyzed on-line and stored on disk or tape for later study.

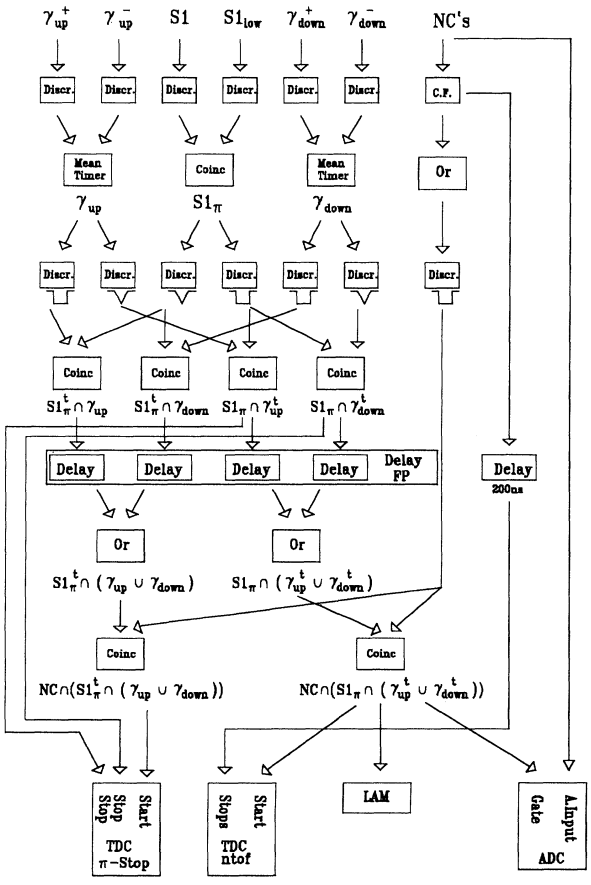

FIG. 2. Schematic layout of the trigger, where t stands for time defining and Delay FP for the delay which accounts for the different flight paths. NC denotes a neutron counter signal and LAM is a CAMAC look-at-me signal.

C. Measurement conditions

The time-of-flight experiment consisted of measurements at two different pressures, 17 and 40 bar, each at two different flight paths, 0.6 and 6.0 m, and a tuning phase with 40 bar at 3.1 m. The pressure was varied to determine the pressure dependence of the kinetic-energy distribution.

The measurement at 0.6 m was used to determine the time resolution of the setup. The TOF of neutrons from a $\pi^- p$ at rest for a flight path of 0.60 m is 67 ns; this corresponds to a neutron kinetic energy of 420 keV ($v = 0.894$ cm/ns). At such a small flight path the influence of the high kinetic-energy components on the TOF is small or even negligible [compare Eq. (9)]. To illustrate this: a neutron emitted toward the neutron detector by a $\pi^- p$ atom with a kinetic energy of 80 eV requires for a flight path of 0.6 m only 1 ns less than a neutron emitted by an atom at rest. The TOF for this flight path was measured at target pressures of 40 and 17 bar to check that the resolution function was independent of possible changes in the stop distribution.

The flight path of 6.0 m was chosen to optimize the visibility of the high kinetic-energy component with respect to the resolution of the apparatus and the count rate.

Before the data taking and during the measurements, the stability of the $S1$, γ_{up}, and γ_{down} electronics was regularly checked for drifts by carefully observing the correlations between $S1$ and the high frequency of the accelerator as well as between $S1$ and γ_{up} or γ_{down}. For both cases, the drifts were less than 1 ns.

The stability of the neutron counter electronics was regularly checked with a calibration setup. This consisted of a ^{207}Bi source and a CsF detector. The ^{207}Bi source emitted x rays with energies at 10 and 70 keV in coincidence with γ quanta of energies of about 500 keV and 1 MeV. The x-ray energies give signals similar to proton recoil signals from 420-keV neutrons. The CsF detector replaced the π^0 counter; it had a time resolution of less than 1 ns. This test setup made it possible to check the TOF electronics for time jitters and drifts. The overall drifts of the neutron counters were measured to be smaller than 1 ns.

The measurements described above and their purposes are summarized in Table I.

D. Data analysis

1. Data reduction

To optimize the peak-to-background ratio and the resolution of the TOF data, three cuts were applied. First, only signals from the ADC spectra of the $S1$ counter were used, which were highly correlated with π^- stopping in the gas target. With this cut, all events coming from an electron triggering the γ_{down} were removed;

TABLE I. The different measurements and their purposes.

Flight path (m)	Target	Purpose	Time duration
3.17	H_2 40 bar	NTOF	14 days
		Check of stability and performance	4 h
	^{207}Bi	Calibration	4 h
6.03	H_2 40 bar	NTOF	3.0 days
		T-distribution pressure dependence	
6.03	H_2 17 bar	NTOF	3.5 days
		T-distribution pressure dependence	
0.62	H_2 40 bar	Resolution function	0.5 days
0.62	H_2 17 bar	Resolution function	0.5 days
	^{207}Bi	Calibration	4 h

this implied a reduction factor of 20 and an improvement of the peak-to-background ratio to 2:1 [compare Figs. 3(A) and 3(B) with Figs. 3(C) and 3(D)]. An energy cut in the γ_{up} and γ_{down} ADC spectra could not be applied due to insufficient energy resolution of the π^0 counters.

Second, the "TDC π-Stop" spectrum was made to select pions stopping in the gas target. This cut ensured that the time spread for the TOF-defining signals is as small as possible. It reduced the background by a factor of 2 and improved the resolution by a factor of 1.5 in addition.

Finally, the ADC signals of the neutron counters were used to optimize further the peak-to-background ratio. The parameters of the cut were determined by the fact that the recoil protons in the scintillator material from monoenergetic neutrons show a boxlike distribution in the ideal case of a single scatter. The peak-to-background ratio improved by a factor 2.

The resulting TOF spectra were corrected for time drifts in each neutron counter during the measuring period by using the bismuth calibration data.

To illustrate how drastically the applied cuts improved the data, two raw TOF spectra at a flight path of 6.0 m are shown in Figs. 3(A) and 3(B). Figures 3(C) and 3(D) show the same TOF spectra after applying the cuts described above.

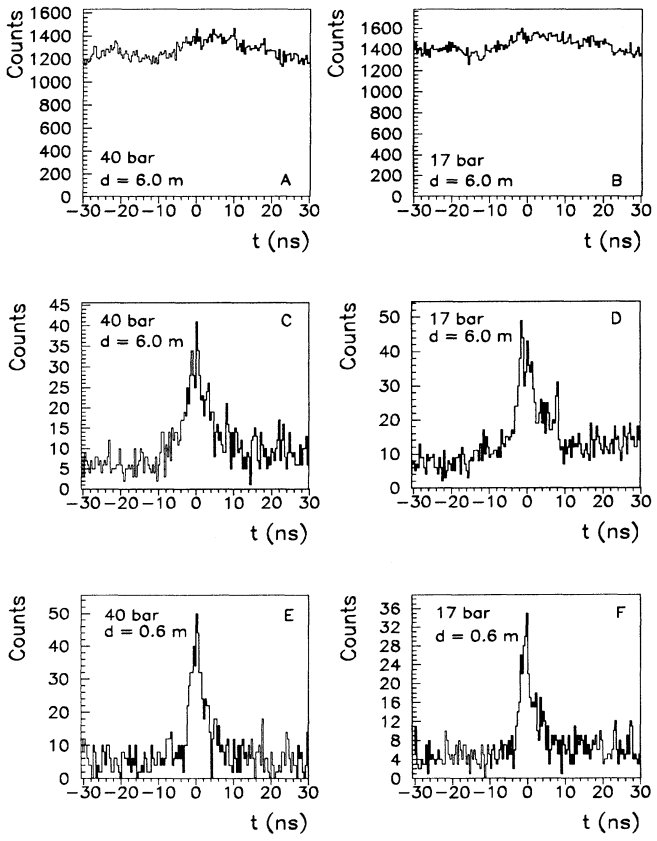

FIG. 3. Neutron time-of-flight data for 40 and 17 bar at 6.0 and 0.6 m [(A) and (B) without cuts, (C)–(F) with cuts].

2. *Background and response function*

After the cuts were applied, the spectra showed a flat background on the left side of the central peak, corresponding to neutrons with kinetic energies higher than $\pi^- p$ atoms at rest. On the right side, however, the data for 6.0-m flight path show a higher overall background. The data for 0.6 m show instead only a tail on the side corresponding to lower energies. Both structures can be explained by elastic scattering of the 420-keV neutrons, as we will now argue.

The relation of final to initial energy for elastic scattering of neutrons at different materials as a function of scattering angle is given by

$$\frac{E_n^f}{E_n^i}=\mu_1^2(\cos\vartheta_n \pm \sqrt{k^{-2}-\sin^2\vartheta_n})^2 , \tag{1}$$

where ϑ_n is the scattering angle in the laboratory system, $\mu_1=m_n/(m_n+m_2)$, $\mu_2=m_2/(m_n+m_2)$, and $k=\mu_1/\mu_2=m_n/m_2$, and m_n, and m_2 are the masses of the neutron or scattering nucleus, respectively.

The experimental setup, depicted in Fig. 4, presented only a few possible scattering centers: the aluminum and iron shielding of the cyclotron magnet around the target [Fig. 4(A)], a 1-mm-thick Al window at the end of the bore hole of the cyclotron trap [Fig. 4(B)], and a lead wall [Fig. 4(C)] with 0.2-m thickness at 1.9-m distance from

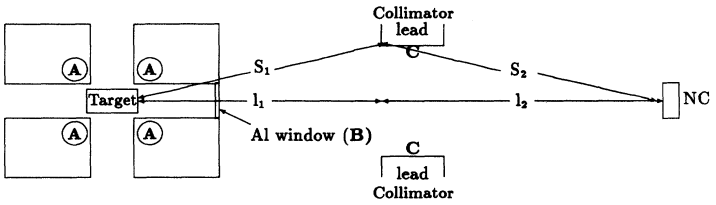

FIG. 4. Schematic layout of the geometry of the possible scattering centers (A), (B), and (C).

the center of the trap. Using relation (1) and referring to the geometry of the setup, we discuss elastic scattering for small and large angles separately.

The influence of elastic scattering at small angles is discussed first. For flight paths of 0.6 and 6.0 m small-angle elastic scattering is possible on the 1-mm Al window, where the largest scattering angles possible are 22° at 0.6 m and 10° at 6.0 m. For the 6.0-m flight path small-angle scattering is also possible on the lead wall, where the largest scattering angle possible is 8°.

Scattering on the Al window results in an energy loss of 3 keV at 0.6 m and 0.6 keV at 6.0 m; the corresponding time difference is about 1 ns for both flight paths. The time difference due to the longer flight path when scattering on the Al window was 1.2 ns for 0.6 m and 0.5 ns for 6.0 m. Scattering on the lead wall with a scattering angle of 8° resulted in an energy loss of 8 keV, leading to a time difference of 13 ns; the time difference due to the longer flight path was 1.5 ns.

Rate estimates showed that the mean value of the central NTOF peak was not influenced by small-angle scattering.

(1) The cross section for 420-keV neutrons to scatter elastically at small angles on the 1-mm Al window, $\sigma_{el}(\mathrm{Al})=5.5471$ b, yields a scattering probability of 3%.

(2) A significant influence on the peak position at 6.0 m from scattering on lead was excluded by solid angle. For neutrons scattered on the lead wall the solid angle was 8.3×10^{-5} sr, a factor 12 less than for unscattered neutrons. These estimates were supported by the fact that the fitted relative peak positions for the different distances (0.6, 3.0, and 6.0 m) agreed with those predicted by the chosen delay times within 200 ps (0.5 channels). Hence small-angle elastic scattering did not explain the observed structure to the right of the peak.

The remaining mechanism to explain the structures on the side corresponding to lower kinetic energies was large-angle elastic scattering. The only source of such scattering was the target region. For example, scattering at 90° produced an energy loss of 15 keV corresponding to a time difference of 2.5 ns at flight path of 0.6 m and 25 ns at 6.0 m. An estimate showed that the solid angle for neutrons scattering in the target region with an angle of 50° is 2.1 sr, about 20% of 4π. The solid angle to reach the neutron counter array after being scattered remains the same as for unscattered neutrons. Therefore, the fraction of such scattered neutrons was significant and can explain the observed structures.

Having understood the background and the position of the central peak, we could obtain the time resolution. The spectra in Figs. 3(E) and 3(F) corresponding to a flight path of 0.6 m were fitted assuming a flat background and a Gaussian shape for the central peak. Due to the structures discussed above, only the left side of the peak was taken into account to extract the FWHM of the Gaussian:

17 bar: 3.22 ns±0.32 ns ,

40 bar: 3.34 ns±0.25 ns .

These values show no significant dependence on pressures; therefore, significant differences in the stop distributions at 40 and 17 bar can be excluded. The resolution is dominated by the 3-ns resolution of the π^0 detectors, which, as shown in Sec. II C, implies that additional effects of high kinetic-energy components on the resolution function can be neglected.

3. *Analysis of the NTOF spectra*

Fitting the NTOF data to obtain the $\pi^- p$ kinetic-energy distribution requires only qualitative knowledge of energy gains and losses in the cascade. Coulomb deexcitation is the only process which can result in energy gains larger than 10 eV. Three Coulomb transitions yield high-energy components in the kinetic-energy distribution: one at 10 eV $\leq T_{\mathrm{middle}} \leq$ 40 eV resulting from the Coulomb transitions 6→5 and 5→4, a second at $T_{75}\sim75$ eV from the Coulomb transition 4→3, and a third at $T_{210}\sim210$ eV from the transition 3→2. The relative fractions of these components change with pressure and the mean kinetic energy $\langle T_{\mathrm{init}} \rangle$ of the initial-energy distribution due to a $1/\sqrt{T}$ energy dependence of this cascade process (see Table III). Kinetic energies less than 10 eV result from the remaining deexcitation processes, such

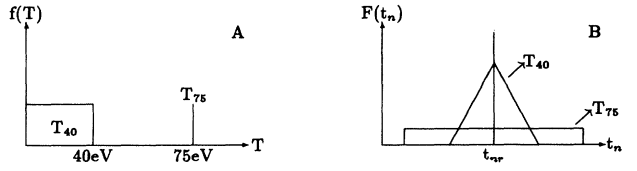

FIG. 5. The simplified $\pi^- p$ kinetic-energy distribution and corresponding TOF distribution used as input to the TOF fits (t_{nr} is the flight time for neutrons coming from a $\pi^- p$ at rest).

TABLE II. The experimental fractions of the different kinetic-energy components at 40 and 17 bar determined from the data shown in Fig. 6. ν_{NDF} is the number of degrees of freedom (NDF).

Pressure (bar)	T_{40} (%)	T_{75} (%)	χ^2/ν_{NDF}
40	73±10%	27±11%	0.9
17	78±9%	22±8%	1.4

as Auger effect, elastic scattering, and radiative transitions.

In Secs. III and IV detailed cascade calculations are presented which show that the kinetic-energy distributions exhibit a rather complicated structure (see Fig. 12). Because of the experimental time resolution of 3 ns, the fits cannot distinguish the structures in the kinetic-energy distribution below 40 eV. For the fits, one continuous component T_{40} was assumed ($0 \leq T_{40} \leq 40$ eV). In addition, we assumed a discrete component at $T_{75} \sim 75$ eV.

The peak-to-background ratio of the present experiment excluded an observation of the high kinetic-energy component at 210 eV. Thus the $\pi^- p$ kinetic-energy distribution due to Coulomb deexcitation could be simplified to the distribution plotted in Fig. 5(A). This simplified distribution can be transformed to a corresponding TOF distribution [Fig. 5(B)] using equations and relations described in the Appendix.

The fractions of the kinetic-energy components were obtained by fitting a TOF distribution [Fig. 5(B)], convoluted with the time resolution function [Sec. II D 2] to the spectra. The measured kinetic-energy fractions and their one sigma errors are listed in Table II. As an example, a fit for 40 and 17 bar is shown in Fig. 6. In Fig. 6 an additional background component is indicated; this could be traced to the 50-Mhz structure of the beam. A detailed discussion of the comparison between these results and the theoretical predictions for the different kinetic-energy components is given in Sec. IV C.

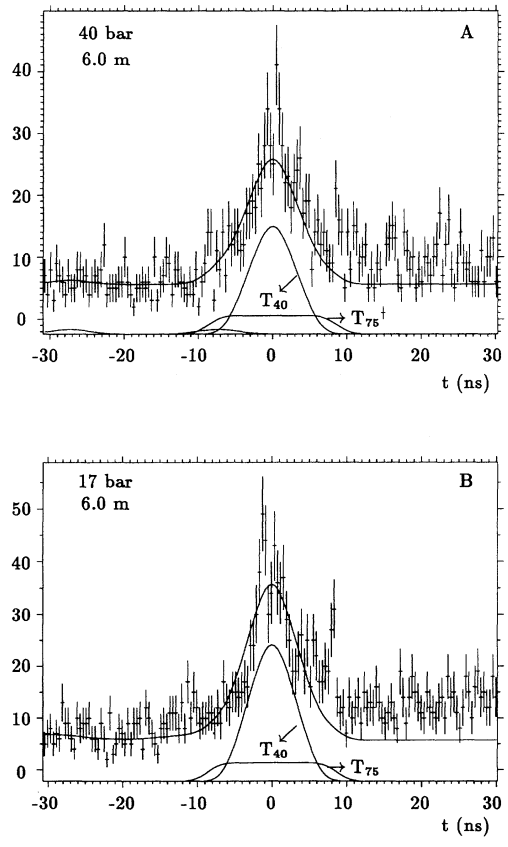

FIG. 6. The fitted neutron time-of-flight distribution for 40 and 17 bar.

III. CASCADE MODEL

The cascade begins with capture of a pion into an atomic orbit. It proceeds from a highly excited state with principal quantum number $n \approx (m_\pi/m_e)^{1/2} \approx 16$ determined by the size of electron Bohr radius a_e. A more elaborate capture model [25], which takes molecular effects into account, predicts that the initial n distribution is peaked near $n = 13$. The characteristic energy of the atom at the instant of formation is assumed to be about 1 eV [25].

The cascade develops mainly via the following processes, which are listed in Table III: radiative deexcitation, external Auger effect, Stark mixing, Coulomb deexcitation, and elastic scattering. The n dependences of the cascade processes are shown in Fig. 7, which are calculat-

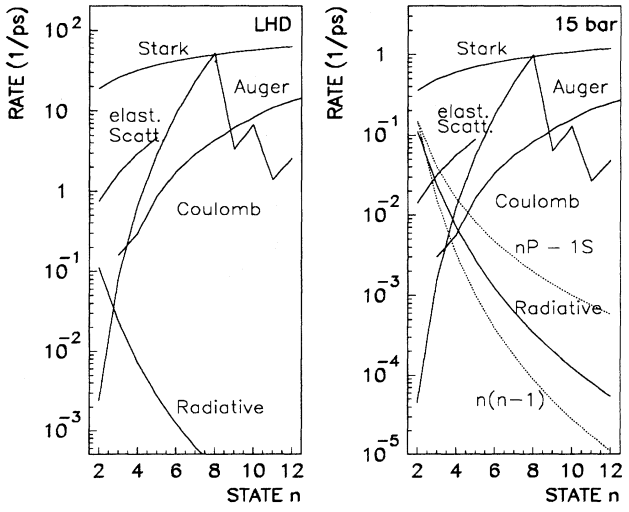

FIG. 7. The rates of various cascade processes vs initial state n for the πp atom at LHD and 15 bar with $T_{\pi^- p} = 1$ eV. The rates of the radiative transitions between circular states $(n,n-1) \rightarrow (n-1,n-2)$ and of the K transitions ($nP \rightarrow 1S$) are shown in addition. Statistical population of the nl sublevels is assumed.

TABLE III. Basic cascade processes and the dependence of their rates on kinetic energy and density.

Process	Energy dependence	Density dependence	Refs.
Radiative $(\pi^- p)_i \rightarrow (\pi^- p)_f + \gamma$	no	no	[19]
Nuclear absorption $(\pi^- p)_{nS} \rightarrow \pi^0 + n, \gamma + n$	no	no	[9,10]
External Auger effect $(\pi^- p)_i + H_2 \rightarrow (\pi^- p)_f + e^- + H_2^+$	no	linear	[1]
Stark mixing $(\pi^- p)_{nl} + H \rightarrow (\pi^- p)_{nl'} + H$	Fig. 8	linear	[1,15]
Coulomb collisions $(\pi^- p)_i + p \rightarrow (\pi^- p)_f + p, n_f < n_i$	$\sim 1/\sqrt{T}$	linear	[16]
Elastic scattering $(\pi^- p)_n + H \rightarrow (\pi^- p)_n + H$	$\sim 1/\sqrt{T}$	linear	[30]

ed for a fixed value $T_{\pi^- p} = 1$ eV. Since the radiative deexcitation rates decrease rapidly with increasing n, only the collisional processes are important at the upper stage of the cascade. The lower the density is, the more significant the radiative transitions are in the deexcitation.

These basic processes are incorporated in the standard cascade model (see [1,3,12,13] and references therein) of hydrogenlike exotic atoms. In this model the kinetic energy of the atom is treated as a fixed fitting parameter used in calculations of the collisional rates.

In order to remove this limitation of the standard model, we used a recently developed cascade computer code [26] which includes the kinetic energy as a time-dependent distribution. We divided the cascade into two stages because only the collisional cascade processes are important above $n = 6$. Since the Coulomb deexcitation and the other collisional processes for $n > 6$ do not produce a significant high-energy component, we assumed the kinetic energy at this stage of the cascade can be characterized by a single parameter, the mean kinetic energy $\langle T_{\text{init}} \rangle$. This kinetic energy is pressure independent above 3 bar, where the radiative transitions are only important for $n < 4$. To test the sensitivity of the theoretical analysis to the distribution, a δ function and Maxwellian distributions were used. We found that both analyses are insensitive to the distributions at our present state of experimental precision (see Table IV). A second important quantity derived from the upper stage of the cascade is the population of the orbital states at $n = 6$. The populations, calculated by the Monte Carlo code, are discussed in Ref. [11].

Below $n = 6$ the evolution of the kinetic-energy distribution was taken into consideration. The pionic hydrogen gains kinetic energy through Coulomb deexcitation and loses through elastic scattering.

In the following we describe some details of the calculations of the cascade processes. The dominant processes in the upper stage of the cascade are Stark mixing, Auger effect, and Coulomb deexcitation. Coulomb deexcitation and elastic scattering as well as radiative transitions dominate the lower cascade.

Stark mixing is the fastest collisional process; the scale of the cross section is determined by the size of hydrogen atom [27]; the rates are monotonically increasing functions of energy and n. The Stark transitions were calcu-

TABLE IV. The theoretically calculated fractions of the different kinetic-energy components at 40 and 17 bar. The cascade model parameters were chosen according to the analysis in Secs. IV A and IV B; we assumed $k_{\text{Cd}} = 1$ throughout. A Maxwellian initial kinetic-energy distribution or a δ-box function initial kinetic-energy distribution were assumed for $n = 6$.

$T_{\pi^- p}$ component	Maxwellian		δ function	
	$\langle T_{\text{init}} \rangle = 1$ eV, $k_{\text{St}} = 2.0$	$\langle T_{\text{init}} \rangle = 2$ eV, $k_{\text{St}} = 1.8$	$\langle T_{\text{init}} \rangle = 1$ eV, $k_{\text{St}} = 2.0$	$\langle T_{\text{init}} \rangle = 2$ eV, $k_{\text{St}} = 1.8$
		$p = 40$ bar		
T_{low}	64	69	66	73
T_{middle}	26	21	24	18
T_{75}	10	10	10	9
		$p = 17$ bar		
T_{low}	70	75	73	80
T_{middle}	23	19	20	14
T_{75}	7	6	7	6

lated in the straight-line trajectory approximation [1] using the dynamical group method [15] by implicit integration over all impact parameters. The result of calculations are shown in Fig. 8. The cross sections thus obtained are about 50% larger than those calculated in the effective impact parameter approximation [1,3]. At low collision energy ($T \sim 1$ eV), one can expect that atomic trajectories deviate significantly from a straight line due to the interaction of the atomic dipole moment with the interatomic electric field. Therefore, the Stark mixing is enhanced by an orbiting effect. In order to account for this effect, we introduced a constant scaling factor k_{St} which was fitted. The Stark mixing rates for the transitions $nS \leftrightarrow nl (l > 0)$ were calculated with the shift and broadening of the nS states taken into account according to [1]. The following values for the shift, including strong interaction and vacuum polarization, and width were used: $\Delta E_{1S} = \Delta E_{1S}^{SI} + \Delta E_{1s}^{VP} = -10.3$ eV [7] and $\Gamma_{1S} = 0.9$ eV [10].

The *Auger deexcitation* rates calculated in the Born approximation [1] are energy independent. The more refined eikonal approximation [28] results in a rather weak energy dependence. Since both methods agree at low n ($n \leq 6$), the former was used in present calculations. The Auger deexcitation is dominated by $E1$ transitions with the minimal change in principal quantum number n possible for the ionization of the hydrogen molecule. The Auger deexcitation rate reaches its maximum at $n = 8$ when transitions with $\Delta n = 1$ become possible. With decreasing n, the Auger rate falls rapidly as the size of the pionic atom becomes much smaller than the electron Bohr radius.

In Auger as well as in radiative processes, the transition energy is carried away mainly by a light particle and the recoil energy of the atom is rather small ($T \ll 1$ eV). In contrast, the transition energy in the Coulomb collisions is divided between the recoil of heavy particles. The transitions between low-lying states result in so-called high-energy components ($T \gg 1$ eV) of the kinetic-energy distribution: the $\pi^- p$ can gain about 30 eV as a result of transition $(n = 5) \rightarrow (n = 4)$, 75 eV for $(n = 4) \rightarrow (n = 3)$, and 210 eV for $(n = 3) \rightarrow (n = 2)$. The rates of the Coulomb deexcitation (Cd) were calculated with the formulas obtained in [16]; no molecular effects were taken into account. The validity of the model [16] was disputed by later calculations [18,17], but more definitive calculations for low-n states ($n \leq 6$) remain to be done. In order to account for uncertainties in the calculations of Coulomb rates, we introduced a second scaling factor k_{Cd}. We discuss the sensitivity of the different measurements to this constant in Sec. IV.

Additional acceleration mechanisms are possible in the upper atomic cascade, e.g., chemical deexcitation [1] and interaction of the atomic dipole moment with the external electric field during the Auger process [18]. Estimates show that these mechanisms can provide acceleration on the scale $T \sim 1$ eV. This is much higher than thermal energy, but less than the acceleration due to Coulomb deexcitation.

During the cascade the atom can lose kinetic energy in *elastic collisions.* Estimates of deceleration rates [29] imply that multiple elastic scattering significantly influences the energy distribution during the cascade. The deceleration due to elastic scattering was calculated in the classical-motion approximation using the exact terms for the Coulomb three-body problem [30]. The deceleration rates shown in Fig. 7 were calculated with transport cross sections at $T = 1$ eV. The energy-dependent differential cross sections were used in the cascade calculations. In the density region considered [$N = (10^{-3} - 1) N_0$] we did not find the results to be very sensitive either to small variations of initial n, or to the initial distribution of l sublevels for a given state n. Insensitivity to the initial n follows from the dominance of collisional transitions with $\Delta n \leq 3$ in the beginning of the cascade; the fast Stark mixing provides a statistical distribution over l.

All cascade calculations were done with a Monte Carlo universal program recently developed for the simulation of the kinetics of muon catalyzed fusion [26]. For a given set of parameters k_{St}, $\langle T_{init} \rangle$, and k_{Cd}, 10^5 chains of the events were generated. This number provided sufficient statistical accuracy for a comparison of the calculations with the available experimental data on x-ray yields and NTOF.

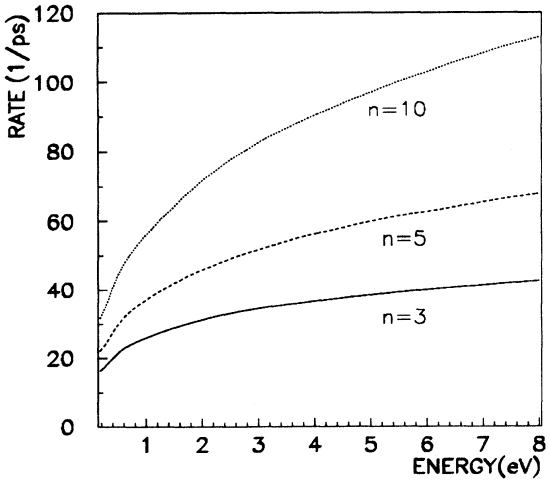

FIG. 8. The energy dependence of the Stark mixing rates calculated for πp atoms in liquid hydrogen [1,15].

IV. EXPERIMENTAL CONSTRAINTS ON THE CASCADE MODEL PARAMETERS

To determine the parameters of the cascade model, we used results from the experiments on x-ray yields [11] and the NTOF measurement in liquid hydrogen [8]. The x-ray yields established a correlation between k_{St} and $\langle T_{init} \rangle$. They are insensitive to the high kinetic-energy components, because only the competition between absorption and radiative deexcitation influences the yields. Since absorption takes place only from ns levels, the competition is dominated by the Stark effect, which populates

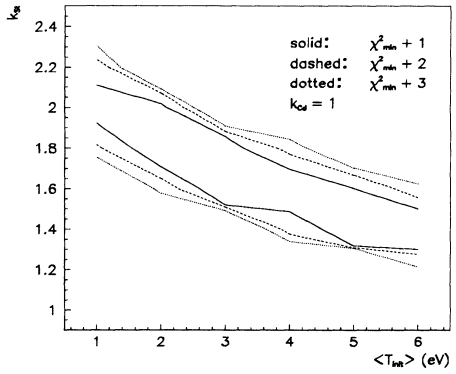

FIG. 9. The χ^2 contour plot vs Stark mixing factor k_{St} and mean kinetic energy at $n=6$ from the fit of the total K lines form Ref. [11] (with $k_{Cd}=1.$).

the ns and nl ($l \geq 1$) levels. The magnitude of the Stark effect depends on $\langle T_{init} \rangle$ as can be seen in Fig. 8. The NTOF data in liquid hydrogen places a strong limit on $\langle T_{init} \rangle$ and restricts k_{Cd}. The NTOF data in gaseous hydrogen were used to cross check on the parameters obtained from the other two experiments.

A. X-ray yields

We studied the dependence of the K-shell x-ray yields on gas pressures with the cascade code, and compared the results with the experimental data on the total K lines at 3, 15, and 40 bar; for details see Ref. [11]. These studies evidenced the strong correlation between k_{St} and $\langle T_{init} \rangle$ shown in Fig. 9. The results were obtained with Coulomb deexcitation rates derived from Ref. [16] ($k_{Cd}=1$); they depend only weakly on the initial shape of

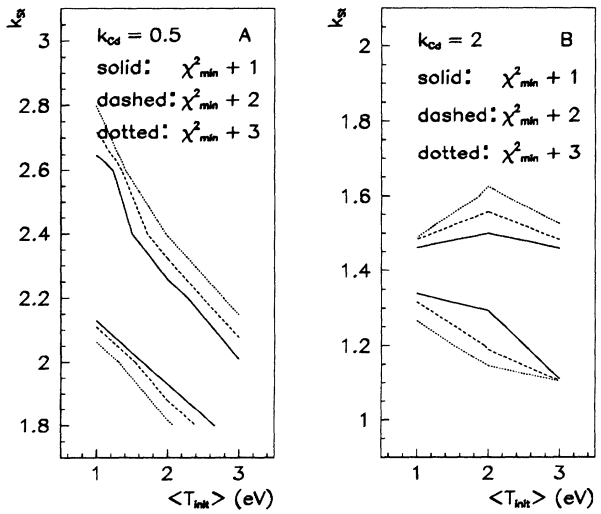

FIG. 10. The χ^2 contour plots vs Stark mixing factor k_{St} and mean kinetic energy at $n=6$ from the fit of the total K lines [11], with Coulomb rates of $k_{Cd}=0.5$ (A) and $k_{Cd}=2.0$ (B).

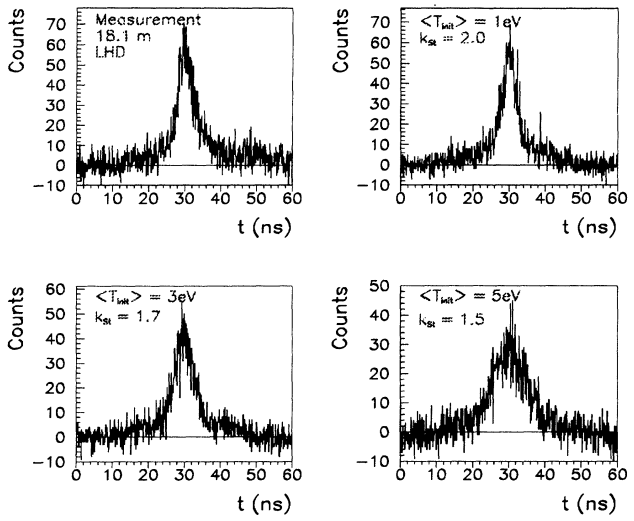

FIG. 11. Comparison of the data (A) from Ref. [8] at a flight path of 18.1 m with simulated NTOF spectra (B), (C), and (D) for different parameter sets of k_{St} and $\langle T_{init} \rangle$ and the resulting kinetic-energy distribution at liquid-hydrogen density.

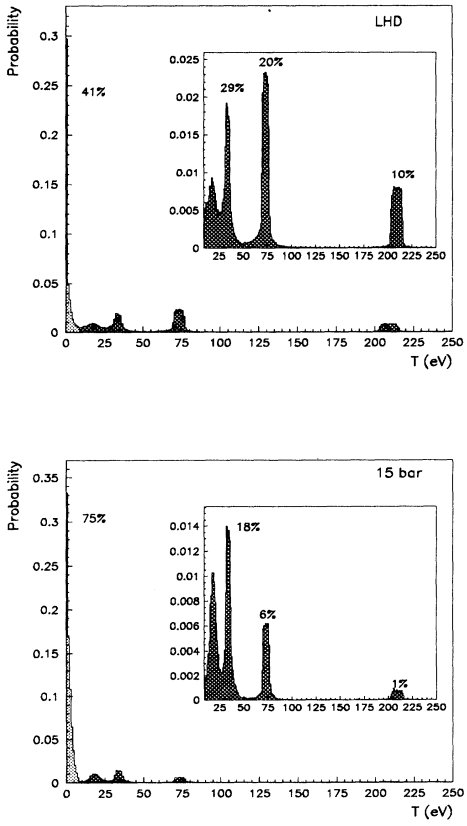

FIG. 12. The kinetic-energy distribution of $\pi^- p$ at the instant of the nuclear absorption in liquid and gaseous (15 bar) hydrogen ($\langle T_{init} \rangle = 2$ eV, $k_{St}=1.8$, and $k_{Cd}=1$).

the energy distribution at $n=6$.

To check the dependence of the correlation on the Coulomb deexcitation rates, we varied these rates in the cascade calculations. The results are shown in Fig. 10, a χ^2 contour plot for the Stark mixing factor k_{St} vs $\langle T_{init} \rangle$, with Coulomb rates a factor 2 smaller [Fig. 10(A)] and a factor 2 larger [Fig. 10(B)] than those in Fig. 9. Figures 10(A), 10(B), and 9 show that the Coulomb rates could be restricted if the Stark mixing rates were well known. For example, a factor $k_{St}=1.8$ would exclude Coulomb rates smaller than those of Ref. [16].

B. NTOF experiment in liquid hydrogen

The results of the cascade calculations for the kinetic-energy distribution were compared with the NTOF data in liquid hydrogen [8]. In Fig. 11 are shown simulations of the NTOF spectra based on the theoretically calculated kinetic-energy distribution folded with a time resolution of 2 ns determined from the experimental spectra [8].

A comparison of Figs. 11 (A) and 11(D) showed that a NTOF spectrum due to a kinetic-energy distribution with $k_{St}=1.5$ and $\langle T_{init} \rangle=5$ eV yields a too broad central peak. Comparison of Figs. 11(A) and 11(C) reveals that decreasing $\langle T_{init} \rangle$ from 5 to 3 eV results in a central peak which is still too broad. However, Fig. 11(B) agreed very well with the measured data, showing that the NTOF data at liquid-hydrogen density are well described by an initial Maxwellian distribution of $\langle T_{init} \rangle=1-2$ eV. (Strictly speaking, this experiment yields an upper limit to $\langle T_{init} \rangle$ of 1–2 eV.) The kinetic-energy distributions are insensitive to the Stark parameter.

Taking the restricted model parameter set, $\langle T_{init} \rangle=2$ eV (Maxwellian energy distribution) and $k_{St}=1.8$, we calculated the kinetic-energy distribution of the atoms at the instant of the nuclear reaction $\pi^- p \rightarrow \pi^0 n$ in liquid hydrogen and at 15 bar. The calculated kinetic-energy distribution is shown in Fig. 12; the peak at low energy results from the initial kinetic-energy distribution at $n=6$, and the peaks at higher energies correspond to the respective Coulomb transitions.

In Ref. [8] the measured kinetic-energy distribution was assumed to consist of two continuous components $f_{low}=0.56\pm0.013$ for $T \leq 0.94\pm0.13$ eV and $f_{high}=0.44$ for $0 \leq T \leq 71.5\pm6.1$ eV [Fig. 13(A)].

Figure 13 shows the theoretical calculated fraction f_{high} of the high kinetic-energy component (1 eV $< T_{high} <$ 70 eV) for varied Coulomb rates and different $\langle T_{init} \rangle$ (solid: $\langle T_{init} \rangle=1$ eV; dashed: $\langle T_{init} \rangle=2$ eV) compared with the experimental results (dotted lines) from Ref. [8]. The figure shows that Coulomb rates according to Refs. [17,18] would be in drastic disagreement with the observed Doppler broadening of the NTOF in

TABLE V. The experimentally obtained and theoretically calculated fraction of the kinetic-energy component T_{75} at 40 and 17 bar. The cascade model parameters were $\langle T_{init} \rangle=2$ eV, $k_{St}=1.8$, and $k_{Cd}=1.0$.

Pressure (bar)	T_{75} (%) Experiment	Theory
40	27±11	10
17	22±8	7

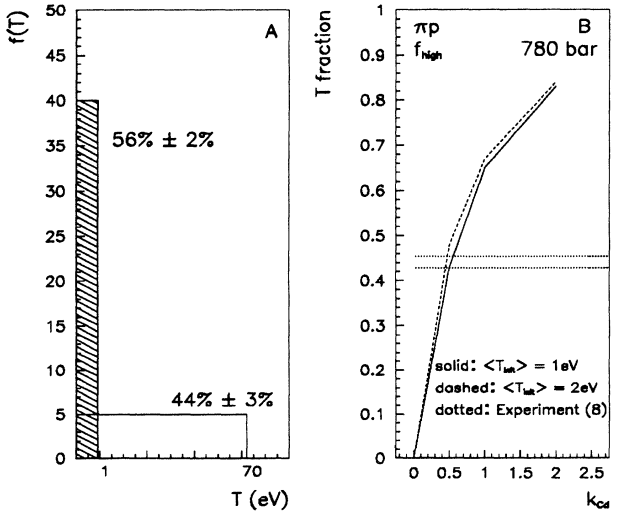

FIG. 13. The kinetic-energy distribution (A) assumed in Ref. [8] and the fraction of the high kinetic-energy component f_{high} for different Coulomb rates in comparison with the result from Ref. [8].

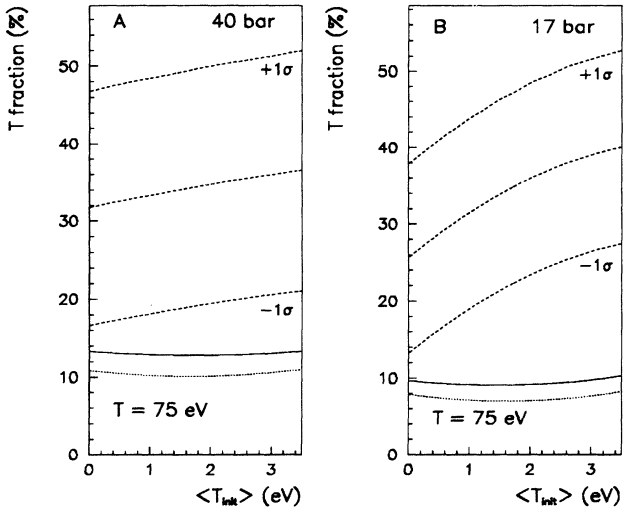

FIG. 14. The calculated high-energy fraction at the instant of the nuclear absorption (solid: $k_{St}=1.4$, dotted: $k_{St}=2.0$) at 40 and 17 bar vs the mean kinetic energy of $\pi^- p$ at $n=6$ in comparison with the results of the fits to the TOF data (dashed lines, best value and $\pm1\sigma$).

TABLE VI. The χ^2/ν_{NDF} for the theoretical obtained time-of-flight distributions shown in Fig. 15.

Pressure (bar) \ k_{Cd}	0.5	1.0	2.0
40	1.3	1.1	0.9
17	1.8	1.6	1.4

liquid hydrogen. With Coulomb rates calculated according to Ref. [16], we found $k_{Cd}=0.5\pm0.2$. For this comparison we neglected the high kinetic-energy component at 210 eV and renormalized the remaining components.

C. NTOF experiment in gaseous hydrogen

To compare the experimental results on the $\pi^- p$ kinetic-energy distribution obtained in Sec. II D 3, the theoretical kinetic-energy distribution was calculated with the constraints on the cascade model parameters from the other experiments. The theoretical results and the experimentally obtained kinetic-energy components are summarized in Table V. Within two standard deviations the data for gaseous hydrogen are consistent with the predictions of the cascade model and the analysis of the x-ray yields and the NTOF liquid data.

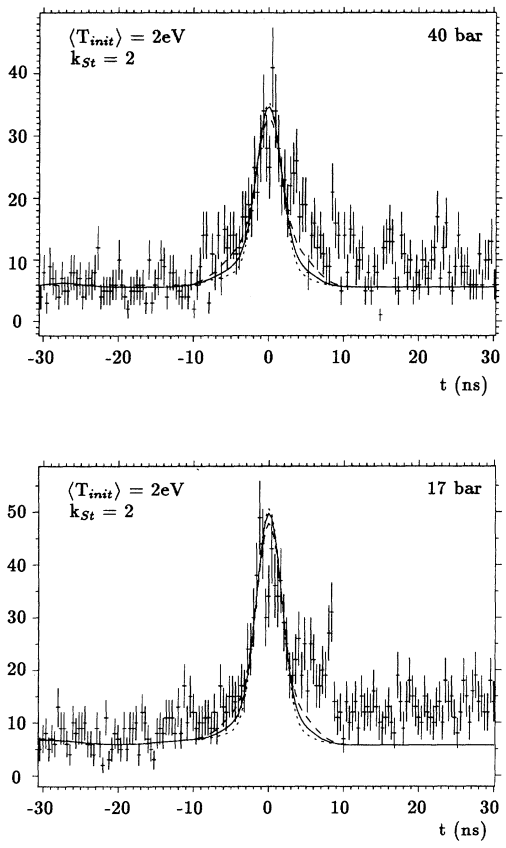

FIG. 15. Neutron time-of-flight data for 40 and 17 bar together with a theoretical time-of-flight distribution with $\langle T_{init}\rangle=2$ eV, $k_{St}=2.0$, and $k_{Cd}=0.5$ dotted line, $k_{Cd}=1.0$ solid line, and $k_{Cd}=2.0$ dashed line. For the evaluation only the left side of the peak was taken into account (see Sec. II D 2).

To show the dependence of the kinetic-energy components on the Stark mixing rates, the Stark parameter was varied in the theoretical calculations as well as $\langle T_{init}\rangle$. Figures 14(A) and 14(B) show the T_{75} component as a function of $\langle T_{init}\rangle$ for two Stark parameters, $k_{St}=1.4$ (solid line) and 2.0 (dotted line). We conclude that the high kinetic-energy components depend much more weakly on the Stark mixing rates than the yields (see Fig. 9).

In spite of the fact that no satisfactory agreement exists between the NTOF spectrum at 17 bar [Fig. 15(B)] and the prediction of the cascade model, we have tried to find out if some preference is given by the data as to a higher or a lower value of k_{Cd}. In order to do this we varied the magnitude of the Coulomb rates in the cascade calculations. In Fig. 15 the theoretical TOF distribution convoluted with the experimental time resolution is plotted with the experimental data for 40 and 17 bar. The theoretical TOF distribution was obtained from a calculated kinetic-energy distribution with the parameter set: $\langle T_{init}\rangle=2$ eV, $k_{St}=2.0$, and $k_{Cd}=0.5$ (dotted line), $k_{Cd}=1.0$ (solid line), and $k_{Cd}=2.0$ (dashed line). The χ^2/ν_{NDF} for each of these fits is given in Table VI. Figure 15 and Table VI show that the agreement between experiment and calculations is marginally worse for the smaller Coulomb rates. This is consistent with our conclusion from the NTOF measurement in liquid hydrogen that Coulomb rates of Refs. [17,18] are in disagreement with the experimental NTOF data.

V. DISCUSSION AND CONCLUSION

A. Cascade processes and kinetic-energy distribution

We have shown that the cascade model presented in Sec. III is in fair agreement with the discussed experimental data for pionic hydrogen over a density region from 3 to 780 bar. To reproduce the absolute K-line yields and the NTOF data, three parameters were introduced: the Stark mixing factor k_{St}, the initial mean kinetic energy $\langle T_{init}\rangle$ at $n=6$, and a correction factor for the Coulomb deexcitation rates k_{Cd}.

From the analysis of the NTOF experiment with liquid hydrogen we found an upper limit for $\langle T_{init}\rangle$ of 1–2 eV. This value is compatible with $\langle T_{init}\rangle$, which was found in the muonic hydrogen diffusion experiment 31–33. This experiment measured the kinetic energy of the muonic atoms in the ground state by observation of μd and μp diffusion in gas [31,32]. The characteristic kinetic energy was measured to be $T\approx2$ eV for the μp atom and $T\approx1$ eV for the μd atom in the pressure range between 47 and 750 mbar. It can be demonstrated [14] that the energy distribution observed for muonic atoms in the ground state under these conditions is developed before reaching the state $n\approx5$, because the collisional processes, which produce high kinetic energies, dominate in this pressure range only at states $n>6$. Because of the similarity of the cascades in muonic and pionic hydrogen, we expect

$\langle T_{\text{init}} \rangle$ to be the same and take the upper limit of 1–2 eV to correspond to $\langle T_{\text{init}} \rangle$ in $n=6$ in pionic hydrogen.

From the analysis of the K-line yields (Sec. IV A) and the kinetic-energy fraction at 780 bar (Secs. IV B and IV C), we found the other cascade model parameters to be $k_{\text{St}}=2.3\pm0.3$ (compare Fig. 9) and $k_{\text{Cd}}=0.5\pm0.2$ when based on the rates calculated according to Ref. [16].

We used the scaling factor k_{St} to account for the enhancement of the Stark mixing due to an orbiting effect: at low collision energies ($T\sim1$ eV), the atomic trajectories are expected to deviate significantly from straight lines due to the interaction of the atomic dipole moment with the interatomic electric field. The value of k_{St} was fixed by fitting the x-ray yields with the mean kinetic energy $\langle T_{\text{init}} \rangle$ prescribed by the analysis of the NTOF experiment in liquid hydrogen.

A refined analysis of the NTOF data at liquid-hydrogen density could improve the estimates on the Coulomb deexcitation rates. Specifically, realistic assumptions about the structures of the kinetic-energy distribution should be incorporated. Improved measurements in gaseous hydrogen pressures are also desirable in order to investigate the n dependence of the Coulomb collision rates. In addition, improved cascade calculations are extremely desirable which treat the rates for Stark mixing, Coulomb deexcitation, and elastic scattering with a common approach.

B. The influence of the high-energy component on the x-ray spectroscopy

The measurement of x rays of pionic hydrogen is the main method for investigating the pion-nucleon interaction at zero energy [9,10]. The final goal of a series of current experiments at PSI [7,20] is to determine the $1s$ level strong interaction shift ϵ_{1s} to a precision of 1% and the absorption width Γ_{1s} to 10%. In order to measure the energy of the x-ray transition ($3P\rightarrow1S$) with an accuracy of 25 ppm, a high-resolution experiment with a crystal spectrometer has been performed [20]. The evaluation of the strong interaction width in this and similar experiments requires knowledge of the Doppler broadening of the x-ray line due to the finite kinetic-energy distribution of the pionic atom at the instant of the nuclear reaction.

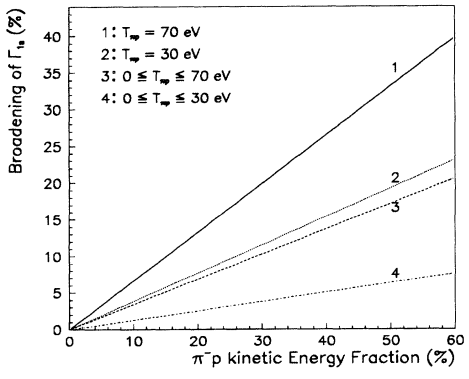

FIG. 16. The percentage broadening of the Γ_{1s} width for different assumptions of the shape and fraction of a single high kinetic-energy component (1 and 2: discrete peaks; 3 and 4: rectangular distribution).

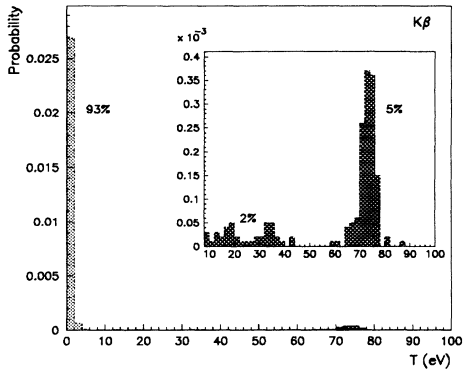

FIG. 17. The kinetic-energy distribution of π^-p at the instant about the x-ray transition at 15 bar for K_β with $\langle T_{\text{init}} \rangle=1.5$ eV, $k_{\text{St}}=2.3$, and $k_{\text{Cd}}=0.5$.

The Doppler broadening is given by the formula

$$\Delta E_x = E_x \left[\frac{2\bar{T}_{\pi^-p}}{M_{\pi^-p}} \right]^{1/2} \tag{2}$$

where ΔE_x is the maximal Doppler shift, E_x is the transition energy of the x ray, and $\bar{T}_{\pi^-p}$ the mean kinetic energy of the π^-p atoms. For a Lorentzian shape, the additional broadening of the x-ray line with respect to the strong interaction width (0.8 eV) of the $1s$ state for different assumptions about the high kinetic-energy components in the initial state is demonstrated in Fig. 16. The relation between the fractions of the high kinetic-energy components and the additional broadening was deduced by folding a Lorentzian line shape with distributions derived from the discrete or continuous high kinetic-energy components labeled 1–4 in Fig. 16.

Using the cascade model described above with the parameters determined from the x-ray yields and NTOF data analysis, we calculated the π^-p kinetic-energy distribution at the moment of radiative deexcitation. Figure 17 shows the kinetic-energy distribution for the $3p$ state relevant to the width measurement at the instant of the K_β transition at 15 bar.

The kinetic-energy distribution at the $3p$ state has a distinctive discrete high-energy component at 75 eV arising from a Coulomb transition $4\rightarrow3$ of 5% preceding the radiative deexcitation and a continuous component of 2% up to 40 eV. This kinetic-energy distribution was obtained from a theoretical calculation with best values of the cascade code parameters $\langle T_{\text{init}} \rangle=1.5$ eV, $k_{\text{St}}=2.3$, and $k_{\text{Cd}}=0.5$.

For the current experiment at PSI to measure the strong interaction width and shift of the $1s$ state [20], the 75-eV component of 5% implies a 4% correction to the measured linewidth.

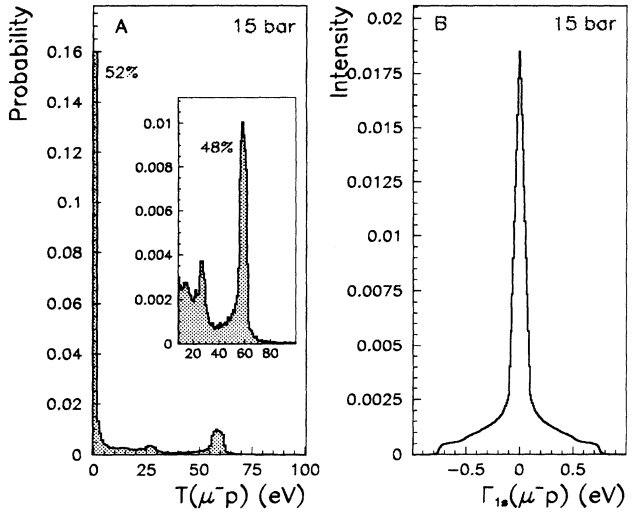

FIG. 18. The $\mu^- p$ kinetic-energy distribution at 15 bar at the instant of the K_β x-ray transition (A) and the $1s$ linewidth after Doppler broadening due to the kinetic-energy distribution in (A).

C. Improved and alternative methods for studying high kinetic-energy components

Experimental knowledge of the $\pi^- p$ kinetic-energy distribution can be improved by a new NTOF measurement with better resolution and statistics. Resolution of about 1.5 ns together with a factor of 5 more statistics would make possible separation of the different single kinetic-energy components. The resolution of this experiment was dominated by the time resolution of the π^0 detector (compare Secs. II A 2 and II D). Improved resolution could be achieved by a π^0 detector with BaF_2 as scintillating material. This would improve the time resolution by a factor of 2.

A second possibility would be to measure the linewidth of the $\mu^- p$ $1s$ state with a crystal spectrometer as in Ref. [20]. The negligible width of the $\mu^- p$ $1s$ state would be broadened by the kinetic-energy distribution as plotted in Fig. 18(A) to a multicomponent profile. The profile shows a characteristic central peak and a high-energy pedestal with a significant spreading up to ± 0.8 eV.

The resulting shape and width of the $1s$ state are shown in Fig. 18(B) for an infinitely good apparatus resolution. This would be a direct measurement of the $\mu^- p$ high kinetic-energy fraction at the $3p$ level, permitting a direct test of calculations of Coulomb collisions rates. Because the Coulomb collision rates scale with the reduced mass of the exotic atom, it tests calculations for pionic hydrogen as well as for $\mu^- p$.

ACKNOWLEDGMENTS

We are grateful to Dr. M. Daum and Dr. R. Frosch for providing us with their data for some aspects of our analysis. We thank the SINDRUM group for loaning us the neutron detector array, and, specifically, Dr. C. Niebuhr for his assistance. Further, we thank Dr. M. Grossmann and Dr. D. Maden for their assistance in solving computer problems and the PSI staff at the cyclotron for providing us excellent beam conditions.

APPENDIX: NECESSARY RELATIONS FOR THE DATA EVALUATION

Before describing the procedure of fitting a high kinetic-energy component of the TOF data, the equations linking the $\pi^- p$ kinetic energy distribution to the corresponding time-of-flight distribution are mentioned.

If the $\pi^- p$ atoms are assumed to move with isotropically distributed velocities $\beta_{\pi^- p}$ of constant absolute magnitude $\beta_{\pi^- p}=(1-\gamma_{\pi^- p}^{-2})^{1/2}$ immediately before the charge-exchange reaction takes place, the neutron TOF distribution dN/dt_n for a given flight path l can be calculated [35]:

$$\frac{dN}{dt}=\frac{l^2}{2\beta_{\pi^- p}\gamma_{\pi^- p}\beta_{\rm nr}\gamma_{\rm nr}(t^2-l^2)^{3/2}}\ , \tag{A1}$$

where $\gamma_{\rm nr}=(1-\beta_{\rm nr}^2)^{-1/2}(v_{\rm nr}=c\beta_{\rm nr})$ is the nonrelativistic relation of the neutron velocity for $\pi^- p$ atoms at rest. The flight time limits are defined by

$$\begin{aligned} t_n({\rm min})&=\frac{l(1+\beta_{\pi^- p}\beta_{\rm nr})}{\beta_{\rm nr}+\beta_{\pi^- p}}\ , \\ t_n({\rm max})&=\frac{l(1-\beta_{\pi^- p}\beta_{\rm nr})}{\beta_{\rm nr}-\beta_{\pi^- p}}\ . \end{aligned} \tag{A2}$$

Together with Eq. (A1), the mean value of the time distribution is given by

$$\bar{t}_n=\int_{t_n({\rm min})}^{t_n({\rm max})}\frac{dN}{dt}t_n dt_n=\frac{l}{\beta_{\rm nr}}=t_{\rm nr}\ . \tag{A3}$$

This mean flight time is exactly equal to the flight time

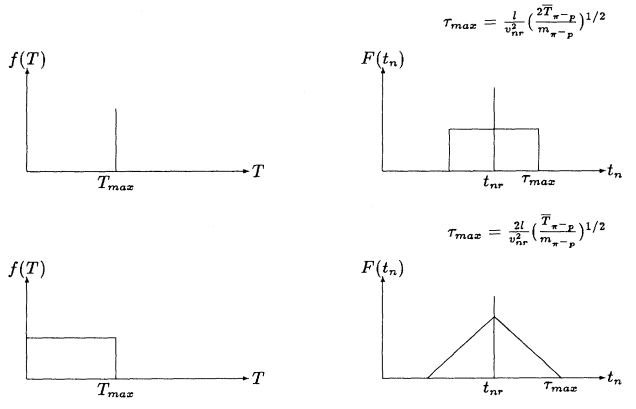

FIG. 19. Two examples of $\pi^- p$ kinetic-energy distributions and their corresponding TOF distributions.

t_{nr} for $\pi^- p$ atoms at rest. If $\beta_{\pi^- p} \ll \beta_{nr} \ll 1$, the time spectra described in Eq. (A3) can be well approximated by a flat spectrum

$$\frac{dN}{dt} = \frac{\beta_{nr}^2}{2l\beta_{\pi^- p}} , \tag{A4}$$

with the limits

$$t_n(\min) = \frac{l}{\beta_{nr}} \left[1 - \frac{\beta_{\pi^- p}}{\beta_{nr}} \right] ,$$
$$t_n(\max) = \frac{l}{\beta_{nr}} \left[1 + \frac{\beta_{\pi^- p}}{\beta_{nr}} \right] . \tag{A5}$$

This leads to the following TOF distribution $F(\tau') = dN/d\tau$:

$$F(\tau') = \frac{\beta_{nr}^2}{2l} \left[\frac{m_{\pi^- p}}{2} \right]^{1/2} \int_{T_{\min}(\tau')}^{\infty} \frac{f(T_{\pi^- p})}{\sqrt{T_{\pi^- p}}} dT_{\pi^- p} . \tag{A6}$$

Here $\tau' = t_n - t_{nr}$, which corresponds to the deviation from the mean flight time. $T_{\min}(\tau')$ is given by

$$T_{\min}(\tau') = \frac{m_{\pi^- p} \beta_{nr}^4 \tau'^2}{2l^2} . \tag{A7}$$

Equations (A6) and (A7) lead to a general relation between the mean kinetic energy of the $\pi^- p$ atoms, $\bar{T}_{\pi^- p} = \int_0^{\infty} f(T_{\pi^- p}) T_{\pi^- p} dT_{\pi^- p}$, and the standard deviation $\sigma_{\tau'}$ of the time distribution $F(\tau')$:

$$\sigma_{\tau'} = \frac{l}{\beta_{nr}^2} \left[\frac{2\bar{T}_{\pi^- p}}{3m_{\pi^- p}} \right]^{1/2} , \tag{A8}$$

Based on Eq. (A8) in Fig. 19, two examples of kinetic-energy distributions and their corresponding TOF distributions are shown.

[1] M. Leon and H. A. Bethe, Phys. Rev. **127**, 636 (1962).
[2] M. Leon, Phys. Lett. **35B**, 413 (1971).
[3] E. Borie and M. Leon, Phys. Rev. A **21**, 1460 (1980).
[4] J. Bailey, A. Placci, E. Polacco, E. Zavattini, K. Ziock, G. Carboni, U. Gastaldi, G. Gorini, G. Neri, and G. Torelli, Phys. Lett. **B33**, 369 (1970).
[5] A. Forster, E. Bovet, J. Gimlett, H. E. Henrikson, D. Murray, R. J. Powers, P. Vogel, F. Boehm, R. Kunselman, and P. L. Lee, Phys. Rev. C **28**, 2374 (1983).
[6] E. Bovet, L. Antonuk, J.-P. Egger, G. Fiorucci, K. Gabathuler, and J. Gimlett, Phys. Lett. **153B**, 231 (1985).
[7] W. Beer, M. Bogdan, P. F. A. Goudsmit, H. J. Leisi, A. J. Rusi El Hassani, D. Sigg, St. Thomann, W. Volken, D. Bovet, E. Bovet, D. Chattellard, J.-P. Egger, G. Fiorucci, K. Gabathuler, and L. M. Simons, Phys. Lett. B **261**, 16 (1991).
[8] J. E. Crawford, M. Daum, R. Frosch, B. Jost, P.-R. Kettle, R. M. Marshall, B. K. Wright, and K. O. H. Ziock, Phys. Lett. B **213** 391 (1988); Phys. Rev. D **43**, 46 (1991).
[9] S. Deser, M. L. Goldberg, K. Baumann, and W. Thirring, Phys. Rev. **96**, 774 (1954).
[10] R. Koch, Nucl. Phys. A **448**, 707 (1986); T. Ericson and W. Weise, *Pions and Nuclei* (Clarendon, Oxford, 1988).
[11] A. J. Rusi El Hassani, W. Beer, J.-F. Gilot, P. F. A. Goudsmit, H. J. Leisi, S. Thomann, W. Volken, E. C. Aschenauer, K. Gabathuler, L. M. Simons, E. Bovet, J. P. Egger, G. Fiorucci, and V. E. Markushin, Z. Phys. A (to be published).
[12] V. E. Markushin, in *EM Cascade and Chemistry of Exotic Atoms,* edited by L. M. Simons, D. Horváth, and G. Torelli (Plenum, New York, 1990), p. 73.
[13] F. Kottmann, in *Muonic Atoms and Molecules,* edited by L. A. Schaller and C. Petitjean (Birkhäuser, Basel, 1993), p. 219.
[14] V. E. Markushin (unpublished).
[15] J.-L. Vermeulen, Nucl. Phys. B **12**, 506 (1969).
[16] L. Bracci and G. Fiorentiti, Nuovo Cimento **43A**, 9 (1978).
[17] W. Czaplinski, A. Gula, A. Kravtsov, A. Mikhailov, N. Popov, and S. Ovchinnikov, Muon Catal. Fusion **5/6**, 59 (1990).
[18] L. I. Menshikov, Muon Catal. Fusion **2**, 173 (1988).
[19] H. A. Bethe and E. E. Salpeter, *Quantum Mechanics of One- and Two-Electron Atoms* (Academic, New York, 1957).
[20] A. Badertscher, M. Bogdan, P. F. A. Goudsmit, L. Knecht, H. J. Leisi, H. Ch. Schröder, D. Sigg, Z. G. Zhao, D. Chattellard, J.-P. Egger, E. Jeannet, E. C. Aschenauer, K. Gabathuler, L. M. Simons, and A. J. Rusi El Hassani, Nucl. Instrum. Methods **335A**, 470 (1993); πN Newsl. **8**, 169 (1993).
[21] L. M. Simons, Phys. Scr. **22**, 90 (1988).
[22] A. J. Rusi El Hassani, W. Beer, J.-F. Gilot, P. F. A. Goudsmit, H. J. Leisi, S. Thomann, and W. Volken, Nucl. Instrum. Methods Phys. Res. Sect. A **290**, 109 (1990).
[23] C. Niebuhr *et al.*, Phys. Rev. D **40**, 2796 (1989).
[24] F. W. Schlepuetz, IEEE Trans. Nucl. Sci. **36**, 1630 (1989); D. T. Jost and D. Vermeulen, *ibid.* **39**, 186 (1992).
[25] G. Ya. Korenman, V. P. Popov, and G. A. Fresenko, Muon Catal. Fusion **7**, 179 (1992).
[26] V. E. Markushin, E. I. Afanaiseiva, and C. Petitjean, Muon Catal. Fusion **7**, 155 (1992).
[27] T. B. Day, G. A. Snow, and J. Sucher, Phys. Rev. Lett. **3**, 61 (1959).
[28] A. P. Bukhvostov and N. P. Popov, Sov. Phys. JETP **55**, 12 (1982).
[29] L. I. Menshikov and L. I. Ponomarev, Z. Phys. D **2**, 1 (1986).
[30] V. I. Savichev (unpublished).
[31] J. B. Kraiman, G. Chen, P. P. Guss, R. Siegel, W. Vulcan, R. Welsh, W. Breunlich, M. Cargnelli, P. Kammel, J. Marton, J. Zmeskal, F. Hartmann, C. Petitjean, A. Zehnder, J. Reidy, and H. Woolverton, Phys. Rev. Lett. **63**, 1942 (1989).
[32] D. J. Abbott, J. B. Kraiman, R. Siegel, W. Vulcan, D. W.

Viel, C. Petitjean, A. Zehnder, W. Breunlich, P. Kammel, J. Marton, J. Zmeskal, J. Reidy, H. Woolverton, and F. Hartmann, in *Muonic Atoms and Molecules,* edited by L. A. Schaller and C. Petijean (Birkhäuser, Basel, 1993), p. 243.
[33] V. E. Markushin, Phys. Rev. A **50**, 1137 (1994).
[34] R. Frosch, Paul Scherrer Institute, Internal Report No. TM-37-21, 1985 (unpublished).